Electrochemomechanical simulations of 3D-resolved solid-state lithium-ion battery cells

M. Alberghini[1], G. Blanco[1], A. Bertinetti[1], A. Tommasi[1]
1. Gemmate Technologies, Turin, Italy.

Abstract

Solid-state batteries have emerged as a cost-effective alternative to traditional liquid-based lithium-ion batteries. However, their implementation still poses several challenges, such as complex electrochemical processes and structural integrity. Numerical simulations represent a key tool to address these issues by optimizing battery cells architecture. In this context, this work presents a microstructure model for solid-state cell at the microscale level, providing insights into their performance and aiming to assist their design. The cell performance was simulated considering the coupled interactions of electrochemistry, heat transfer, and mechanics and, then, compared to that of a standard electrode setup; additionally, the electrolyte tortuosity and cathode electrical conductivity were also evaluated. The results obtained were used to evaluate how different microstructure assumptions affect the cell performance and possible mechanical damage. In future works, these results can be used to calibrate 1D and 0D models, facilitating the evaluation of battery performance over extended cycles and incorporating aging effects.

Keywords: Lithium-ion batteries; Microscale modeling; Electro-chemo-mechanics; 3D-resolved microstructure

1. Introduction

Numerical simulations are a powerful tool to understand the impact of the coupled physical phenomena controlling battery performance and to optimize their design at the microstructure level. However, capturing the elaborate 3D cell structure while compromising between accuracy and computational cost presents a significant challenge: on the one hand, accurate geometries can be derived from experimental data such as FIB-SEM images; on the other hand, simplified models may be inadequate to represent crucial transport phenomena in detail.

This work presents a novel design approach that aims to improve the representation of 3D-resolved electrodes while avoiding high computational costs of reconstructing complex geometries. Instead, all electrode components are automatically generated from basic shapes such as spheres, cubes, and cylinders; these geometries match the target volume fractions of each component, the particle size distributions of the active material, and, importantly, aim to capture the effects of the carbon black (CB) networks.

This approach is an important improvement with respect to several well-established works [1, 2, 3], which generally assume an overlap between the active material particles and homogeneous distribution of CB in the electrolyte. Balancing accuracy and simplicity, the proposed approach aims to provide a more accurate model of battery cathodes.

The concept is applied to a solid-state argyrodite-based cell: the simulation setup is presented in Section 2; the mathematical model, boundary conditions and solution procedure are presented in Section 3; and, finally, Section 4 compares the main simulation results with those obtained from a conventional simulation setup generated considering the same microstructure parameters.

2. Simulation Set Up

The simulation setup, shown in Fig. 1A, was built following the experimental manufacturing parameters and procedures used for laboratory-level argyrodite-based coin cells. The cell anode was modelled as an ideal lithium plate; instead, the cathode was modelled as composed by a mixture of NMC811 (purple spheres), commercial carbon-based additive SuperP (CB, black spheres), and argyrodite sulfide (Li_6PS_5Cl) as a solid electrolyte (SE). The SE was modelled as a continuous homogeneous medium (grey domain within the cathode); instead, the NMC particles were supposed to preserve their original particles size distribution (PSD), namely particles with diameters in the range $2\,\mu m - 11\,\mu m$.

Finally, the CB was modelled with particles with diameter in the range $0.25\,\mu m - 0.75\,\mu m$. The electrodes are separated by a thick layer of argyrodite (green domain), while the cathode is connected to an aluminum plate; the cross section of the simulation domain was set to $20\,\mu m \times 20\,\mu m$. The volume fractions of the cathode components, and the thicknesses of the cathode and separator are summarized in Tab. 1. The resulting cell architecture provides a nominal capacity of 1.47 mAh/cm^2.
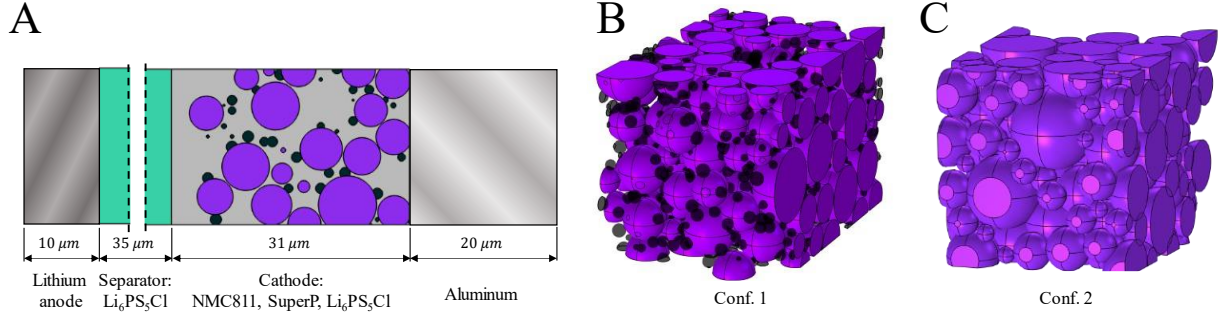
A

B

C

Conf. 1

Conf. 2

Figure 1: (A) Schematic of the simulated solid-state battery cell, highlighting the materials included and the thickness of each component. (B-C) Comparison of the generated cathode microstructures representative of the solid state cell, highlighting the NMC (purple spheres, panels B-C) and SuperP (black spheres, panel B) domains. The setup shown in panel C does not explicitly represent CB aggregates, which are instead assumed to be homogeneously distributed in the SE, and allows for NMC particle overlap. The simulation setup represents a 20 μm×20 μm cross section.

In panel A labels: 10 μm, 35 μm, 31 μm, 20 μm; Lithium anode, Separator: Li_6PS_5Cl, Cathode: NMC811, SuperP, Li_6PS_5Cl, Aluminum.

Component	Density (g/cm^3)	Volume fraction (-)	Thickness (μm)
NMC811	4.87	0.49	-
SuperP (CB)	1.89	0.05	-
Li_6PS_5Cl, catholyte	1.64	0.46	-
Total cathode	3.16	-	31.3
Li_6PS_5Cl, separator	1.64	1.00	35.0
Li anode	0.53	-	10.0
Aluminum	2.70	-	20.0

Table 1: Cell components included in the model.

The cathode microstructures represented in Figs. 1B-C were modelled as an ensemble of spheres, representative of the active material and the aggregates of the CB conductive additive, if present. The packing of NMC spheres was obtained by a fall-and-roll approach [4]. The text files containing the NMC and CB coordinates were imported into COMSOL Multiphysics® and used within a Method script to automatically build a representative portion of the cell. As the complexity of the cathode structure required a large number of objects (3000+ spheres), the CAD import module was used to ease the geometry generation. The microstructure was generated explicitly avoiding contact between neighboring NMC particles, as lithium transport between adjacent active material particles would be overestimated by neglecting the misalignment between the crystal lattices and the non-ideality of the contact between the particles would be predicted by a more conventional model. Therefore, note that lithium intercalation at the NMC-SE interface can only occur if the particles belong to a NMC-CB network with a direct connection to the positive current collector. This hypothesis allows to include more realistically the effects of microstructure properties in the 3D model, and highlights the crucial role of CB in determining the cell performance. As mentioned above, the cell performance was compared with that of a cell obtained by considering overlapping NMC particles and the CB as homogeneously dispersed in the cathode SE, resulting in the electrolyte being modeled as a conductive porous domain (see Fig. 1C). The NMC

particles were allowed to overlap of about 1 μm, in agreement with experimental characterizations reported in the literature [1]. Note that coupling between solid mechanics and electrochemistry was neglected in this second setup. For the sake of simplicity, the configuration with explicit CB aggregates (see Fig. 1B) will be referred to as Conf. 1, while the configuration with CB homogeneously dispersed in the SE and overlapping particles (see Fig. 1C) will be referred to as Conf. 2.

3. Governing Equations and Numerical Model

3.1. Solid mechanics:
Mechanical stresses and deformations were evaluated within the cell domain in the quasi-static approach and assuming linear elastic models for the simulated materials. The displacement field was discretized using quadratic elements; note that the elements should be of at least second order to evaluate the derivative of stress fields.

The effect of intercalation strain ϵ_{ic} was evaluated for the NMC particles as:

$$\epsilon_{ic} = \frac{1}{3}\frac{\Delta W}{W_0}\boldsymbol{I},$$

where $\boldsymbol{I}$ is the identity matrix, and $\Delta W/W_0$ is the concentration-dependent volumetric strain related to intercalation evaluated from the COMSOL material library definition of NMC811.

Mechanical stresses affect the electrochemical cell behavior by (i) modifying the equilibrium potentials and (ii) introducing a convective term in the transport equation of Li within the NMC, both described in the Sections below. These interactions are both functions of the local hydrostatic stress, defined as:

$$\sigma_h = -(\sigma_x + \sigma_y + \sigma_z)/3,$$

where $\sigma_{x,y,z}$ are the diagonal components of the stress tensor. Note that the sign of σ_h was reversed with respect to its conventional definition: this can be understood by analysing the stresses of an ideal NMC particle surrounded by the SE homogenously losing a given amount of lithium during charging. The intercalation strain forces the particle to shrink; at equilibrium, the stresses required to achieve this

configuration are compressive, exerted by the SE on the NMC surface. However, the particle should instead be in traction, with the electrolyte (assumed as tightly bonded) attempting to counteract the particle shrinkage. Note that this analysis holds only for intercalation-induced stresses, while the conventional sign holds for external stresses applied to the cell.

Incorporating the aluminum plate proved essential to maintain consistent stress levels within the NMC at the positive current collector. This choice was preferred over employing "fixed" or "roller" boundary conditions, which tend to counteract the volume reduction resulting from lithium de-intercalation and can lead to large and non-physical stresses. The cell was initially supposed as non-deformed and stress-free. The lateral surfaces of the simulation domain were allowed slide via a roller boundary condition, while the outer lithium and aluminum surfaces were supposed to be fixed. The required mechanical properties of the cell materials are reported in Tab. 2.

3.2. Electrochemistry:

The electrochemical performance of the cell was determined by solving the charge conservation equations in the SE, NMC and CB domains and the mass conservation of Li in the NMC domains. For simplicity, the anode was assumed to be an iso-potential component, and therefore was represented in the electrochemical model only by its reactive boundary; the separator, similarly with the SE in the cathode, was modelled as a homogenized and electrically insulating layer, while the current collectors, normally considered as iso-potential components, were not included in the model. The unitary transference number of the SE allows to consider it a single-ion conductor, which allows to neglect the concentration-induced polarization losses in the electrolyte. The intercalation-induced current i at the NMC-SE and anode-SE interfaces was modelled via the Butler-Volmer equation within the Internal Electrode Surface interface.

The concentration-dependent equilibrium potential V at the NMC-SE interface was evaluated as:

$$V = V_0 + \frac{\Omega \sigma_h}{F},$$

where V_0 is the concentration-dependent equilibrium potential of the active material evaluated from the COMSOL material library definition of NMC811, and Ω is the partial molar volume of the active material, defined as:

$$\Omega(c) = \frac{d}{dc}\left(\frac{\Delta W}{W_0}\right),$$

where $\Delta W / W_0$ was evaluated from the library model of the NMC811.

Charge and discharge cycles were simulated by imposing a fixed specific current density at the interfaces between the positive current collector and both the NMC and CB, defined as:

$$i = \pm H(t)I,$$

where I was ranged between $C/20$ and $C/2$, being C the C-Rate of the cell, $+I$ and $-I$ were respectively used for charge and discharge cycles, $H(t)$ is the smoothed Heaviside step function, centered at 0.05 s and with a width of 0.05 s, which was added to grant numerical stability at the beginning of each cycle. When stable performance was achieved for each value considered (that is, when the initial and final cell SOC remained constant over multiple cycles) the applied current was gradually increased. Note that the SE was assumed to be as an ideal electrical insulator. Cyclometric tests performed on NMC cells are commonly performed setting the upper and lower cut-off potentials to 4.2 V and 3 V, respectively. However, the NMC equilibrium potential sharply decreases as $c/c_{max} \rightarrow 1$: to grant numerical stability, the lower cut-off potential was set to 3.364 V. Finally, symmetry was assumed on all the lateral surfaces of the setup.

The electrochemical model was implemented using the Battery Design module, with single-ion conductor selected as the charge balance model. To reduce computational complexity, the electric and electrolyte potentials were linearly discretized. The models included in the COMSOL Multiphysics® material library for the NMC811, lithium metal and graphite were used. All the physicochemical parameters required by the model are reported in Tab. 2.

3.3. Convection-diffusion of Li in NMC:

Lithium transport within the NMC particles was modelled with a convection-diffusion equation:

$$\frac{\partial c}{\partial t} + \nabla \cdot (-D\nabla c + \boldsymbol{\beta} c) = 0,$$

where c is the local concentration of Li in the NMC microparticles, D is the diffusion coefficient of lithium and $\boldsymbol{\beta}$ is the convection coefficient due to concentration-induced pressure gradients within the particles, defined as:

$$\boldsymbol{\beta} = \frac{D\Omega(c)}{RT} \nabla \sigma_h .$$

where σ_h is the local hydrostatic stress and Ω is the partial molar volume of the active material, both defined above. Note that, coherently with several literature references [5, 6, 7], D was set to $4.2 \cdot 10^{15}$ m²/s and approximately two orders of magnitude lower that that reported in the COMSOL Multiphysics® material library.

The convection-diffusion equation was modelled relying on a Coefficient Form PDE interface. The initial lithium concentration in the NMC was set to $c_{max}SOC_{max}$. The boundary flux of lithium due to intercalation at the NMC-SE interface was evaluated as i/F. Instead, a no-flux condition was applied to the remaining surfaces. All the physicochemical parameters required by the model are reported in Tab 2.

3.4. Thermal transport:

The temperature evolution of the cell was modelled by means of a 1D thermal model, representing the cross section of a coin cell with radius equal to 7 mm. In particular, the cell was assumed to exchange heat with the environment (at a fixed temperature of 25 °C) by natural convection. The cell averaged thermal capacity was evaluated as a mass-weighted average of the individual component thermal capacities, while the average thermal conductivity was evaluated by considering the cell as an equivalent series of thermal resistances. The heat generated by the cell during operation Q_{3D} was evaluated from the electrochemical model and considered as a uniform volumetric heat source within the entire 1D cell domain, namely:

$$Q_{1D} = Q_{3D} \frac{n \, L_c}{L_{tot}},$$

where Q_{3D} was evaluated as the volume average of the irreversible heat generated in the NMC, $n = 1$ is the number of cells in series simulated, L_c is the cathode thickness, and L_{tot} is the total cell length, including the thickness of the current collectors, here both assumed to be 10 µm thick. Note that, to grant numerical stability, the '*nojac*' operator was applied to the volumetric heat source Q_{1D}. The resulting average cell temperature was used to update the transport properties and insertion reaction of the materials involved via the Arrhenius equation.

The thermal model of the coin cell was implemented via the Heat Transfer in Solids interface, applied to a separate 1D component. All the parameters required by the thermal model are reported in Tab. 2.

SuperP (CB)

Poisson's Ratio (-)	0.33
Young's Modulus (GPa)	0.5
Electrical Conductivity, σ (S/m)	100
Thermal conductivity (W/m/K)	1

Lithium Anode

Poisson's Ratio (-)	0.34
Transfer Coefficient, α (-)	0.50
Reference Exchange Current Density, i_0 (A/m^2)	0.10
Molar density, M (g/mol)	6.94

NMC811

Poisson's Ratio (-)	0.3
Young's Modulus (GPa)	138
Electrical Conductivity, σ (mS/m)	1.7
Transfer Coefficient, α (-)	0.5
Maximum concentration, c_{max} (mol/m^3)	50060
Maximum state of charge, SOC_{max} (-)	0.942
Minimum state of charge, SOC_{min} (-)	0.222
Solid Diffusivity, D (m^2/s)	$4.2 \cdot 10^{-15}$
Reference Exchange Current density, i_0 (A/m^2)	1.526
Thermal conductivity (W/m/K)	1.58

Argyrodite (SE)

Poisson's Ratio (-)	0.35
Young's Modulus (GPa)	26
Electrical Conductivity, σ (mS/m)	2.05
Initial concentration (mol/L)	20
Transference number (-)	1

Cell thermal properties

Specific heat capacity (J/kg/K)	1150
Density (kg/m^3)	1615
Thermal conductivity (W/m/K)	0.65

Table 2: physicochemical parameters required to run the simulations.

3.5. Electrolyte tortuosity and cathode electrical conductivity:

To evaluate the electrolyte tortuosity, the Laplace equation was solved only considering the SE domain within the cathode, simulating the diffusion of a fictive species u with unitary diffusion coefficient and bounded concentration in the range between 0 and 1. Dirichlet boundary conditions were imposed at both ends of the cathode; the tortuosity τ was computed by evaluating the normalized stationary species flux J flowing through the SE:

$$J = \left| \frac{L_c}{A} \int (-\nabla u \cdot \mathbf{n}) \, dA \right|; \quad \tau = \frac{\phi}{J},$$

where ϕ is the electrolyte volume fraction within the cathode, L_c is the cathode thickness, and A is the cross sectional area of the simulation domain, here $A = 20 \, \mu m \times 20 \, \mu m$.

Similarly, the electrode conductivity was evaluated by solving the steady state charge conservation equation in the electron-conducing domains (namely, the CB and NMC), implemented via a coefficient form PDE in the form:

$$\nabla \cdot (-\sigma \nabla \phi) = 0.$$

By imposing a fixed different in the electric potential $\Delta \phi$ across the cathode via Dirichlet boundary conditions, the effective cathode conductivity can be evaluated as from the boundary current as:

$$\sigma_{eff} = \left| \frac{L_c}{A \, \Delta \phi} \int (-i \cdot \mathbf{n}) \, dA \right|.$$

3.6. Solver setup via Method scripting:

The physical processes governing the cell performance are inherently time-dependent; however, the computational cost of solving the solid mechanics at each time step, despite the quasi-static assumption, would have been too demanding. Therefore, a Method script was used to automatically manage and run the simulations, alternating the time-dependent solution of the electrochemistry, lithium transport and 1D thermal problem with the steady-state simulation of the solid mechanics. The script requires an input parameter, expressed in seconds, that defines the frequency of the solid mechanics simulations; the transport properties function of the hydrostatic stress are updated after each stationary
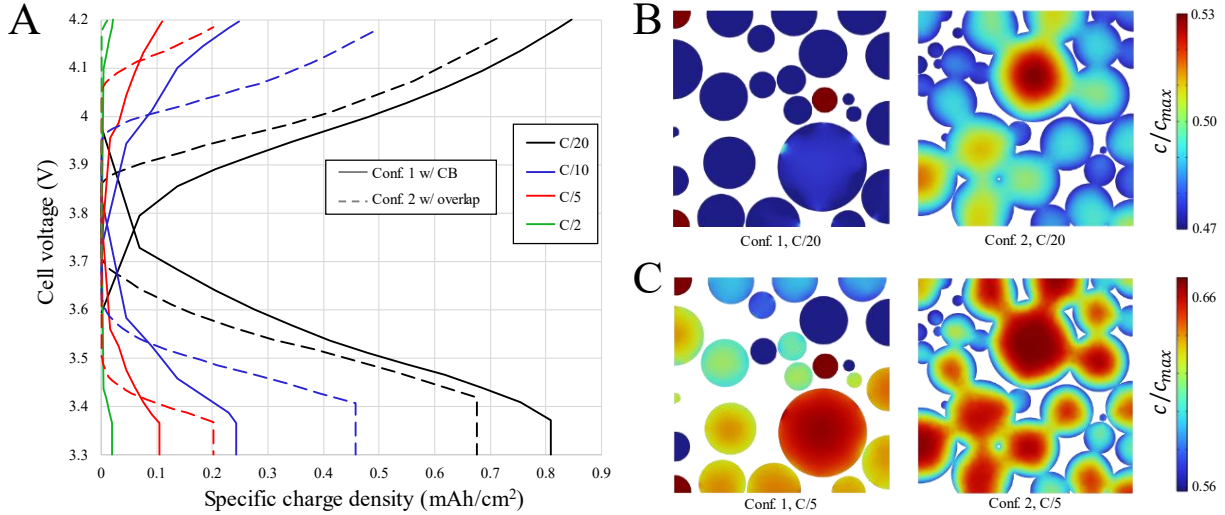
Figure 2: (A) Comparison between the cell characteristics obtained with the two microstructure configurations simulated at different C-rates. The results of the configuration with explicit CB aggregates, labeled Conf. 1, are shown with solid lines, while those with homogeneous CB and overlapping particles, indicated as Conf. 2, are shown with dashed lines. (B-C) Comparison of the relative lithium concentration within the NMC particles of the two microstructures at C/20 (panel B) and C/5 (panel C). The reported cross-sections were evaluated at 5 μm from the positive current collector.

simulation and assumed to be constant until the next solid mechanics simulation is run. The simulation is restarted iteratively until a target end time or cutoff potential is reached. The upper and lower cutoff potentials, defined as global parameters, are automatically set as the stop condition whether the cell is charging or discharging. Once the simulation is complete, the script automatically reverses the sign of the applied current density, allowing the following charging/discharging cycle to be performed by simply rerunning the method script. Consistently with the initial conditions described above, a charge cycle is performed first. A preliminary sensitivity analysis showed that a good trade-off between computational cost and accuracy was achieved by simulating solid mechanics 10 times per cycle.

4. Simulation Results

The model described in Section 3 was used to evaluate the performance of the solid state cells described in Section 2. Considering the standard setup with distributed CB (see Fig. 1C, Conf. 2), the transport properties of both SE and CB are corrected using the Bruggeman approximation, yielding $\sigma_B = \sigma \, \phi_i^{1.5}$, where $\phi_i = \phi_{CB}$ for the conductive additive and $\phi_i = 1 - \phi_{CB}$ for the electrolyte (see Tab. 1). It's important to note that these assumptions consider the two media to be homogeneously mixed, ignoring any possible percolation effects. Moreover, in this second configuration, the influence of stresses on the electrochemical process is also neglected.

To evaluate how the different assumptions affect cell performance, we first compare how the two microstructure assumptions affect cathode tortuosity and the effective electrical conductivity σ_{eff}. To improve the statistical representativeness, the results

of three different configurations generated with the same microstructure parameters were averaged. The inclusion of the CB aggregates in the model (see Fig. 1B, Conf. 1) leads to an electrolyte tortuosity of (1.52 ± 0.02), while the inclusion of the overlap between the NMC particles leads to an increased value of (3.98 ± 0.03). Note that the presence of the CB aggregates spheres plays a minor role on the SE tortuosity with respect to the average NMC distance: removing the CB particles from the electrolyte tortuosity is (1.47 ± 0.03), consistent with the theoretical value predicted by the Bruggeman theory of 1.51 for the same volume fraction and with previous works [8]. The effective electrical conductivities vary by almost an order of magnitude between the two configurations: the inclusion of the CB aggregates leads to $\sigma_{eff} = (1.4 \pm 0.2)$ S/cm, while it increases to (33.0 ± 0.5) S/cm when considering a homogeneously dispersed conductive additive. Interestingly, the electrolyte conductivity of Conf. 1 closely matches the experimental values obtained on similar NMC811 electrodes [9], suggesting that the proposed approach may yield results closer to real cells with similar architecture.

Electrochemical simulations are crucial to understand how the two investigated microstructure models could affect the overall cell performance and influence major design constraints. For the sake of simplicity, the simulations focused only Conf. 1 and Conf. 2. The average energy released by each configuration as a function of the current applied is shown in Tab. 3. The results of the electrochemical simulations highlight the complex interplay between the physics considered and the microstructure models analyzed. The homogeneous distribution of CB in the SE considered in Conf. 2 lead to a higher particle connectivity and electrical conductivity with respect to Conf. 1, which translates into higher
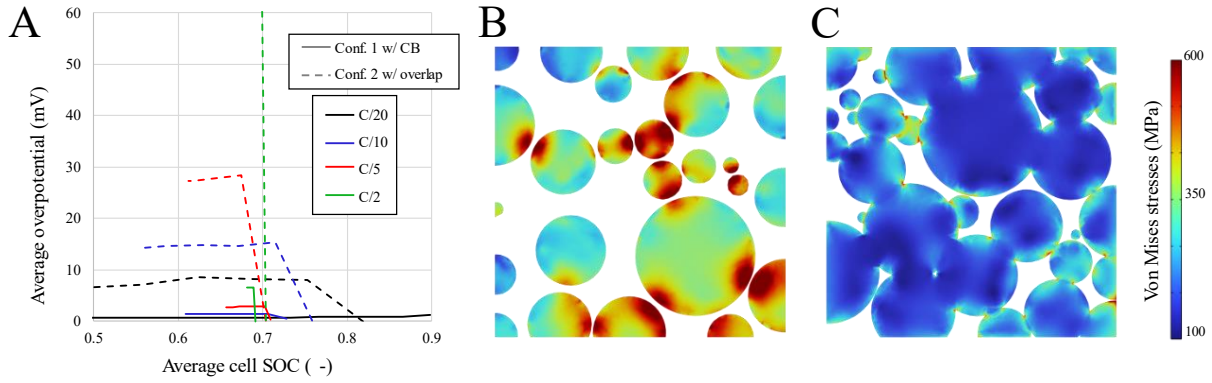
Figure 3: (A) Average cell overpotential as a function of the cell SOC for the different C-rates tested. The results obtained for Conf. 1 are reported with solid lines, while those whit Conf. 2 are shown with dashed lines. (B-C) Von Mises stresses obtained at the end of the charge cycle at C/20 with Conf. 1 (panel B) and Conf. 2 (panel C). Both cross sections were evaluated at 5 µm from the positive current collector.

energy released at C/10 and C/5. However, Conf. 1 performs similarly at C/20 and significantly better at C/2; instead, at the highest current tested, the high losses in Conf. 2 prevent any energy from being released during discharge (see Tab. 3 and Fig. 2A). The causes of this non-trivial and non-monotonic response can be understood by analyzing the influence of several aspects on the electrochemical behavior of the cell.

Energy released (mAh/cm²)

	Conf. 1	Conf. 2
C/20	0.81	0.67
C/10	0.24	0.46
C/5	0.10	0.20
C/2	0.02	0.00

Table 3: Energy released by the two microstructure configurations varying the applied current density.

A key factor is the distribution of Li within the NMC particles: Figs. 2B-C compare the relative Li concentration of both configurations tested at the end of a charge cycle at C/20, where the deepest de-lithiation is achieved, and C/5, the highest current at which both configurations successfully release energy. Note that some of the particles in Conf. 1 are not connected to the positive current collector (red particles) and thus maintain a constant Li concentration since they could not participate in the de-lithiation. The NMC in Conf. 2 shows significant concentration gradients; the larger the particle, the greater the difference between the particle surface and the core, resulting in a suboptimal discharge depth due to uneven distribution; this behavior becomes more pronounced at higher currents. Furthermore, the contact between adjacent particles in Conf. 2 only mitigated this behavior due to the limited diffusion coefficient of Li. In contrast, the inclusion of convective flux due to mechanical stress allows the NMC particles in Conf. 1 with substantially more homogeneous internal Li distribution. However, at higher C-rates all particles in Conf. 2 have similar Li distributions, whereas in Conf. 1, probably due to the limited connectivity to the CB network, larger particles present a

significantly higher amount of Li. This behavior is likely responsible for the poorer performance of Conf. 1 at higher currents, despite having smaller concentration gradients, resulting in a higher SOC after charging than Conf. 2.

This analysis is further supported by the evaluation of the cell average overpotential, which is directly related to the cell efficiency. Fig. 3A shows the overpotential as a function of the average cell SOC during the charge cycles of the two configurations at the different C-rates tested. Conf. 1 always presents significantly lower values of overpotential, in accordance with the reduced concentration gradients within the NMC particles, although the cell capacity is lower than that of Conf. 2 (lower differential values of SOC at the end of each charging cycles, see Fig. 3A). This shows that the hypothesis behind Conf. 1 tends to limit the electrochemical losses mostly due to concentration polarization within the active material: while the concentration of Li in the SE can be neglected thanks to the single-ion conductor hypothesis, the contribution to the overpotential provided by mechanical stress is always less than 2.5 mV.

As expected, higher currents increase the cell overpotential, which limits the insertion kinetic at the SE-NMC interface (via the Buttler-Volmer equation) and, at the limit, does not allow battery operation by blocking insertion currents, as happened in Conf. 2 at C/2. However, the low electrical conductivity of Conf. 1 is more limiting than higher overpotentials at low C-rates; therefore, the two models considered may lead to significantly different estimates of cell performance when considering low or high applied current densities.

A major difference between the two investigated setups is the coupling of electrochemistry and mechanics: the stresses in Conf. 2 are evaluated only at the end of the charge/discharge transients, while in Conf. 1 they are solved at fixed time intervals and used to update the transport equations. Figs. 3B-C uses the von Mises stress to compare the stress state of the active material of both configurations at the

end of the charge at C/20, where the deep lithiation led to the highest stress configuration investigated in this study. Conf. 1 shows an average von Mises stress of 336 MPa, with higher values where the NMC particles are in close proximity. Furthermore, the high stresses are not localized but distributed throughout the particles. Instead, accounting for particle overlap results in lower stresses within the NMC, with an average value of 160 MPa and stress peaks concentrated at the sharp angles where particles are in contact. By increasing the applied currents, both configurations show similar stress patterns, with Conf. 1 having an average Von Mises stress twice that of Conf. 2. When the cell is discharged at C-rates higher than C/20, the final cell SOC does not increase sufficiently to avoid the formation of residual stresses in the order of about 175 MPa and 100 MPa for Conf. 1 and Conf. 2, respectively.

This analysis highlights the importance of coupling mechanics with electrochemistry, as the two physics are deeply connected: evaluating the stresses only at the end of the de/lithiation process leads to an underestimation of the stress state of the cell, and consequently to the possible associated damage and performance degradation.

5. Conclusions

This work compares the performance of two 3D-resolved microstructure models of solid-state Li-ion cells, both including the same components but built under different assumptions. The first, a novel model, explicitly includes a simplified network of conductive aggregates, avoids overlap between particles of active material, and includes mechanical stresses in the evaluation of cell performance. The second, a standard model, assumes that the conductive additive is homogeneously distributed in the electrolyte and allows for particle overlap.

A stark contrast between the two assumptions is that the inclusion of CB particles results in a lower electrical conductivity of the cathode, in the order of 10^0 S/cm and one order of magnitude lower than the standard setup, in agreement with previous experimental results. This translates into a different electrochemical performance: stored and released energy decrease at higher C-rates compared to the standard setup. However, the inclusion of mechanically driven Li transport within the active material particles not only leads to a more homogeneous Li distribution and a significant reduction of the cell overpotential, but also to a higher and more homogeneous stress distribution within the active material particles. The latter result is an indication that there may be a higher level of damage than would be predicted by a more conventional model.

The results presented provide valuable insights into the interaction between different microstructure models and cell performance. The observed discrepancies emphasize the importance of considering microstructural nuances while attempting to improve the accuracy of 3D battery cell models. Future works might use these results to calibrate 1D and 0D models, facilitating the evaluation of battery performance over extended cycles and incorporating aging effects.

References

[1] P. Liu, R. Xu, Y. Liu, F. Lin and K. Zhao, "Computational modeling of heterogeneity of stress, charge, and cyclic damage in composite electrodes of Li-ion batteries," *Journal of The Electrochemical Society,* vol. 167, no. 4, p. 040527, 2020.

[2] W. Mei, Q. Duan, P. Qin, J. Xu, Q. Wang and J. Sun, "A three-dimensional electrochemical-mechanical model at the particle level for lithium-ion battery," *Journal of The Electrochemical Society,* vol. 166, no. 14, 2019.

[3] R. Xu, L. S. de Vasconcelos and K. Zhao, "Computational analysis of chemomechanical behaviors of composite electrodes in Li-ion batteries," *Journal of Materials Research,* vol. 31, no. 18, pp. 2715-2727, 2016.

[4] J. Joos, A. Buchele, A. Schmidt, A. Weber and E. Ivers-Tiffée, "Virtual Electrode Design for Lithium-Ion Battery Cathodes," *Energy Technology,* vol. 9, no. 6, p. 2000891, 2021.

[5] I. McClelland, S. Booth, N. Anthonisamy, L. Middlemiss, G. Pérez, E. Cussen, P. Baker and S. Cussen, "Direct Observation of Dynamic Lithium Diffusion Behavior in Nickel-Rich, LiNi0.8Mn0.1Co0.1O2 (NMC811) Cathodes Using Operando Muon Spectroscopy," *Chemistry of Materials,* 2023.

[6] Z. Geng, Y.-C. Chien, M. Lacey, T. Thiringer and D. Brandell, "Validity of solid-state Li+ diffusion coefficient estimation by electrochemical approaches for lithium-ion batteries," *Electrochimica Acta,* vol. 404, p. 139727, 2022.

[7] Y. Zhao, S. Kucher and A. Jossen, "Investigation of the diffusion phenomena in lithium-ion batteries with distribution of relaxation times," *Electrochimica Acta,* vol. 432, p. 432, 2022.

[8] D.-W. Chung, M. Ebner, D. Ely, V. Wood and E. Garcìa, "Validity of the Bruggeman relation for porous electrodes," *Modelling and Simulation in Materials Science and Engineering,* vol. 21, no. 7, p. 074009, 2013.

[9] R. Tian, N. Alcala, S. O'Neill, D. Horvath, J. Coelho, A. Griffin, Y. Zhang, V. Nicolosi, C. O'Dwyer and J. Coleman, "Quantifying the effect of electronic conductivity on the rate performance of nanocomposite battery electrodes," *ACS Applied Energy Materials,* vol. 3, no. 3, pp. 2966-2974, 2020.

Acknowledgements